Molecular Insights into Species-Specific ACE2 Recognition of Coronavirus HKU5

Yuanyuan Zhang[1,2,3,4†], Yuya Li[2,3,4†], Weijie Gao[2,3,4], Dexin Li[2,3,4], Lingyun Xia[2,3,4,5†*], Qiang Zhou[2,3,4*]

[1]College of Life Sciences, Zhejiang University, Hangzhou, Zhejiang, 310058, China.

[2]Center for Infectious Disease Research, Research Center for Industries of the Future, Zhejiang Key Laboratory of Structural Biology, State Key Laboratory of Gene Expression, School of Life Sciences, Westlake University, Hangzhou, Zhejiang, 310024, China.

[3]Westlake Laboratory of Life Sciences and Biomedicine, Hangzhou, Zhejiang, 310024, China.

[4]Institute of Biology, Westlake Institute for Advanced Study, Hangzhou, Zhejiang, 310024, China.

[5]Present Address: School of Life Sciences, Anhui University, Hefei, Anhui, 230601, China.

[†]These authors contributed equally: Yuanyuan Zhang, Lingyun Xia, Yuya Li

[*]Corresponding author. Email: lyxia@ahu.edu.cn and zhouqiang@westlake.edu.cn

Abstract

Coronaviruses represent a significant zoonotic threat, with host adaptation serving as a pivotal determinant of cross-species transmission. The bat-derived β-coronavirus HKU5 utilizes its spike (S) protein for receptor recognition and viral entry. Here, we report the cryo-electron microscopy (cryo-EM) structure of the HKU5 S protein in a closed conformation. Two fatty acids are found in each protomer of the HKU5 S protein, which stabilize the S protein in the closed conformation. Furthermore, we solve the structure of the HKU5 receptor-binding domain (RBD) in complex with the peptidase domain (PD) of *Pipistrellus abramus* angiotensin-converting enzyme 2 (ACE2), uncovering a unique binding mode distinct from other coronaviruses that use ACE2 as their receptor. Evolutionary and functional analyses indicate that mutations in the RBD can modulate receptor binding, while conservation and structural modeling suggest that HKU5 has the potential to cross the species barrier. Notably, we identify ACE2 orthologs in avian species, such as *Pitta sordida*, that support stable HKU5 RBD binding and interaction. Our functional assays, including pseudovirus entry and cell–cell fusion experiments, demonstrate that HKU5 can exploit ACE2 orthologs across species, providing molecular insights into its host adaptation and underscoring the importance of surveillance for this virus and its zoonotic risk.

Introduction

Coronaviruses (CoVs) are zoonotic pathogens with significant potential for cross-species transmission, exemplified by SARS-CoV[1], MERS-CoV[2] and SARS-CoV-2[3,4]. They often originate from animal reservoirs, especially bats, before spilling over to humans[5-7]. The spike

41 (S) protein of coronaviruses mediates receptor recognition and membrane fusion, with the
42 receptor-binding domain (RBD) typically determining host specificity and spillover potential[8,9].
43 The RBD can adopt an "up" or "down" conformation, where only the "up" state engages
44 receptors[10-12]. These conformational shifts are regulated by various factors, including sialic
45 acids and fatty acids[13-17].
46 Bat coronavirus HKU5 (BatCoV-HKU5) belongs to the β-coronavirus *Merbecovirus* subgenus
47 and is closely related to MERS-CoV[18-20]. Despite being discovered in 2006 and the
48 identification of numerous related sub-clades[21], HKU5 remains relatively underexplored
49 compared to SARS-CoV, MERS-CoV, and SARS-CoV-2. Recent studies have shown that
50 HKU5 can utilize the angiotensin-converting enzyme 2 (ACE2) from *Pipistrellus abramus*
51 (Japanese house bat), *Homo sapiens* (Human) and mink for host cell entry[22-25], which serves
52 as a receptor for multiple coronaviruses, including SARS-CoV[26], SARS-CoV-2[4,27], HCoV-
53 NL63[28], MOW15-22[29,30] and HKU25[31] and has been implicated in repeated spillover events[32].
54 In this work, we determine the cryo-electron microscopy (cryo-EM) structure of the HKU5 S
55 protein in the closed conformation, with each protomer bound with two fatty acids that stabilize
56 this state. We also characterize the interaction between HKU5 RBD and bat ACE2, noting
57 differences from MERS-CoV and SARS-CoV-2. By integrating structural analysis,
58 evolutionary insights, and functional assessment of RBD mutations, we provide a
59 comprehensive perspective on HKU5's host adaptability and spillover risk. These findings
60 contribute valuable knowledge to coronavirus research, with functional validation of receptor
61 usage demonstrating that HKU5 can engage ACE2 from diverse hosts and underscoring the
62 need for ongoing surveillance of this virus and its zoonotic risk.

Results

Structure of HKU5 S protein in the closed conformation

We have over-expressed and purified the HKU5 S protein (UniProt ID: A3EXD0), and then solved its cryo-EM structure at a resolution of 2.4 Å (Supplementary Figs. 1, 2a-d). Unlike the open conformations observed in the S proteins of SARS-CoV-2[11], MERS-CoV[33] or HKU1-B[34], all three RBDs of the HKU5 S protein are in the "down" position (Fig. 1a). This closed conformation hinders interactions with host receptors, potentially delaying host cell entry or facilitating immune evasion[14,35]. Notably, the N174 glycan on the N-terminal domain (NTD) of one protomer forms polar contacts with residues S534, R538, and D549 on the neighboring RBD, which may further stabilize the down state (Supplementary Fig. 2e). In addition, the receptor-binding motif (RBM) is largely buried within the trimer, and the limited exposed surface is masked by glycans from adjacent protomers (N418, N495, and N590), together forming a dynamic glycan shield that reduces the accessibility of the binding interface, a mechanism widely described in coronaviruses.

In the cryo-EM map of the HKU5 S protein, two additional non-protein densities are identified for each protomer. The first one is in a pocket (pocket 1) near the interface between the RBDs of adjacent protomers, while the second one is in another pocket within the RBD (pocket 2), near the RBM (Fig. 1a and Supplementary Fig. 2e). Mass spectrometry experiments suggest the HKU5 S protein contains oleic acid and palmitic acid (Fig. 1b, c and Supplementary Fig. 3), which are fitted to pocket 1 and 2 based on their density shape, respectively (Fig. 1a). The pocket 1 is formed by hydrophobic residues F393, L419, L422, L423, F426, V428, F431, P438, L441, L449, V451, V488, A490, F569, and V571 on the RBD (Fig. 1d). The polar head of oleic

acid interacts with residues Y463, S468, and A469 from an adjacent protomer (Fig. 1d). In a cryo-EM map of the HKU5 S protein with S468A&Y463A double mutant (S_{DM1} protein), the density corresponding to oleic acid was absent, indicating the importance of these polar residues for the interaction with oleic acid (Supplementary Figs. 4, 5). Compared to the wild-type (WT) protein, the S_{DM1} protein exhibited a ~5° clockwise rotation of the NTD (Supplementary Fig. 5a and Supplementary Movie 1), resulting in a looser trimeric assembly[36]. Additionally, the SD1 and SD2 domains shifted away from the RBD toward the NTD, forming new polar interactions such as a salt bridge between R689 of SD2 and D346 of NTD, and a hydrogen bond network involving residues ^{689}RMT^{691} of SD2 and ^{348}GYDD^{351} of NTD (Supplementary Fig. 5b-e and Supplementary Movie 2). These changes were accompanied by structural remodeling, suggesting that oleic acid is beneficial for maintaining the closed conformation of the S protein. This observation parallels findings in SARS-CoV-2, where linoleic acid binding stabilizes the closed state of the S protein[17]. The pocket 2, where the palmitic acid binds, is in the interior of the RBD (Fig. 1e), which has not been reported in any other S protein of coronaviruses. Although the pocket 2 is close to the receptor-binding interface, it does not directly contact it, possibly suggesting a structural or regulatory role in modulating RBD dynamics rather than directly influencing ACE2 binding. To further examine functional effects, we generated pseudoviruses carrying either WT S or the fatty acid binding site mutants, S_{DM1} and S_{DM2} (S457A&Y559A). Infection assays revealed no significant differences in entry efficiency (Supplementary Fig. 5f, g). Together, these results suggest that fatty acid binding plays a role in stabilizing the closed conformation of the S protein, but is not essential for ACE2-mediated entry.

107 **Interaction of HKU5 RBD with bat ACE2**

108 To elucidate the interaction between the HKU5 S protein and ACE2 of its natural host,
109 *Pipistrellus abramus*, we conducted biochemical and structural studies. The S protein in its
110 closed conformation does not co-migrate with the peptidase domain (PD) of the *Pipistrellus*
111 *abramus* ACE2 (*Pa*PD) in gel filtration chromatography, indicating that the closed S trimer
112 cannot directly bind to the receptor (Supplementary Fig. 6). To understand the molecular
113 mechanism underlying HKU5 S protein receptor recognition, we determined the cryo-EM
114 structure of the HKU5 RBD in complex with *Pa*PD at a resolution of 3.2 Å, allowing accurate
115 modeling and analysis (Fig. 2a and Supplementary Fig. 7a-d).

116 The RBM of the HKU5 RBD adopts a compact super-secondary structure comprising a four-
117 stranded anti-parallel β-sheet (β5~β8, residues N504~P560) and a short helix (α4, residues
118 S457~L464), which are critical for receptor recognition and binding (Fig. 2a, b and
119 Supplementary Fig. 7e). The *Pa*PD comprises key structural elements that facilitate its
120 interaction with HKU5 RBD, including the α1 helix (18~54 a. a.), α2 helix (90~101 a. a.), α3
121 helix (322~330 a. a.), a β-hairpin (346~358 a. a.), and a loop region (L_A; 384~399 a. a.) (Fig.
122 2a, b).

123 The interface between the RBD and *Pa*PD spans an area of ~1107 $Å^2$ and can be divided into
124 three patches, each playing a pivotal role in stabilizing the complex. The patch 1 involves
125 interactions between RBD residues from β5 and β6 (E510, Y512, A516, Y517, G518, K519,
126 Y521) and *Pa*PD residues in the α1 helix (R26, E37), α2 helix (D90, Q96), β-hairpin (N353),
127 and L_A loop (N386, S388) (Fig. 2c). The interaction is mediated by eight hydrogen bonds and
128 one salt bridge (Fig. 2c), which collectively ensure the stability of this initial contact point. The

predominance of polar and charged residues highlights the importance of this region in the high-affinity binding observed in the HKU5 RBD–*Pa*PD complex. The residues of patch 2 from β7 and β8 of the RBD (K543, Y544, S546, Y557) interact with *Pa*PD residues from the α1 helix (N38), α3 helix (D329), and β-hairpin (K352, D354) (Fig. 2d). Notably, K543 and Y557 in RBD form a salt bridge and a hydrogen bond with D329 in *Pa*PD, respectively, while Y544 in RBD interacts with D354 and K352 in *Pa*PD. N38 and K352 in *Pa*PD also engage with S546 in RBD through hydrogen bonds (Fig. 2d). Patch 3 incorporates a variety of stabilizing interactions (Fig. 2e). Specifically, D459 in the RBM and Y559 in β8 of the RBD form a salt bridge and a cation-π interaction with R328 in the *Pa*PD α3 helix, respectively. Additionally, hydrophobic interactions are observed in the region encompassing Y463 of the RBD α4, Y507 of RBD β5, and P324 of the *Pa*PD α3 helix. Collectively, these three patches establish a highly specific binding interface between the HKU5 RBD and *Pa*PD, which is crucial for host ACE2 recognition and initiation of viral entry.

In addition to HKU5, numerous other coronaviruses utilize ACE2 for host cell entry, including the epidemic- or pandemic-causing SARS-CoV[26] and SARS-CoV-2[4,27], as well as human coronavirus HCoV-NL63[28], and several bat coronaviruses, such as NeoCoV[37], PDF-2180[37], PRD-0038[38], and MOW15-22[29,30]. The RBM of SARS-CoV-2 forms an accessible, expansive surface that tightly binds human ACE2. HCoV-NL63 RBD has a β-sandwich core with three non-contiguous RBMs clustered at the center. The RBMs of PDF-2180 and MOW15-22 adopt a four-stranded anti-parallel β-sheet similar to HKU5, but HKU5 is more compact with an extended fourth strand (Fig. 2f and Supplementary Fig. 7e).

Structural comparison reveals differences of the HKU5 RBD-ACE2 interface to the other

151 coronaviruses (Fig. 2g). HKU5 shares partial binding footprints with the known modes of
152 SARS-CoV-2, HCoV-NL63, and PDF-2180, but lacks conserved residues among these viruses
153 (Fig. 2g). This indicates that the HKU5 RBD employs a unique interface to interact with ACE2,
154 likely contributing to the host specificity.
155

156 **Evolutionary dynamics of HKU5 RBD**

157 To explore the evolutionary dynamics of the HKU5 RBD, we performed a clustering analysis
158 of the sequences from the NCBI protein database sharing more than 80% identity with the
159 HKU5 S protein (Supplementary Fig. 8). The results show that six HKU5 sub-clades recorded
160 in the NCBI Taxonomy database are distributed across two clusters (Supplementary Fig. 8).
161 Most of the HKU5 RBD residues are highly conserved across various sub-clades, particularly
162 within the core framework of the RBD, indicating their critical role in maintaining structural
163 integrity (Supplementary Figs. 8, 9). However, over 30 variable sites are found in the RBM,
164 particularly spanning the segment Q494~G564 (Supplementary Figs. 8, 9) that accounts for
165 more than two-thirds of the residue indels and point mutations.

166 To evaluate the impact of different HKU5 sub-clades on ACE2 recognition specificity, we
167 employed bio-layer interferometry (BLI) to quantify the *Pa*PD binding affinity of various
168 HKU5 RBD variants (Fig. 3a). The highest affinity is observed for HKU5, with a KD of 19.94
169 ± 0.23 nM. BtPa-BetaCoV/GD2013 (GenBank accession: AIA62343.1) and BatCoV-HKU5-3
170 (GenBank accession: ABN10893.1) display similar binding affinity, at 23.40 ± 0.27 nM and
171 25.17 ± 0.29 nM, respectively. BatCoV-HKU5-related (GenBank accession: QHA24687.1)
172 viruses show a slightly lower affinity, with a KD of 35.24 ± 0.37 nM. These HKU5 sub-clades

173 exhibit *Pa*PD binding affinity either comparable to or slightly lower than that of the HKU5,
174 suggesting that the mutations observed in these variants have only a minor effect on receptor
175 binding.
176 To further investigate the influence of conserved interface residues on the interaction between
177 HKU5 RBD and *Pa*PD, we utilized a tripartite split-fluorescence system[39] in conjunction with
178 flow cytometry to identify potential key residues within the HKU5 RBD (Fig. 3b, c). These
179 assays showed high sensitivity for the interaction of the HKU5 RBD with *Pa*PD, with signal
180 intensity exceeding that of the HKU5 RBD with PD of *Homo sapiens* ACE2 (*Hs*PD), which is
181 a negative control, by more than tenfold (Fig. 3d). Targeted mutations of interface residues
182 revealed that, except for Y544, mutations of the other residues, namely Y463, Y507, Y517,
183 K519, Y521, K543, S546, Y557, and Y559, led to varying degrees of destabilization of the
184 interaction, as evidenced by decreased fluorescence (Fig. 3d). Notably, the K519A mutation
185 caused a reduction in fluorescence intensity by more than 50%. It is important to highlight that
186 residues Y507, K543, Y544, and Y557 are not highly conserved among HKU5 sub-clades (Fig.
187 3d). When these non-conserved residues were mutated to their corresponding residues in other
188 sub-clades, we observed a reduction in fluorescence intensity by approximately 50%, as in the
189 cases of Y507H, K543D, and Y557S (Fig. 3d). These findings contribute to a deeper
190 understanding of the factors influencing the binding affinity of the HKU5 virus for its receptor.
191

192 **Cross-species transmission risk analysis of HKU5**

193 To investigate the potential for cross-species transmission of HKU5, we conducted a detailed
194 structural analysis of the *Pa*PD residues recognized by HKU5. We introduced point mutations

195 at several polar residues of *Pa*PD that are likely to stabilize the interface, including R26A,
196 E37A, Q96A, N321A, P324A, W327A, R328A, D329A, K352A, N353A, D354A, and S388A
197 (Fig. 4a). Tripartite split-fluorescence experiments performed on these mutants revealed that
198 most of the mutations resulted in a noticeable reduction in relative fluorescence intensity,
199 indicating their significant contribution to the virus–receptor interaction (Fig. 4b). Notably, the
200 R328A mutation in *Pa*PD caused a reduction in relative fluorescence intensity to below 50%.
201 The R328 in *Pa*PD stabilizes the interface through a salt bridge with D459 and a cation-π
202 interaction with Y559 in HKU5 RBD, thus maintaining the interaction between HKU5 and
203 *Pa*PD (Fig. 2e). This result aligns with the reduced fluorescence intensity observed in the
204 HKU5 RBD Y559A mutant (Figs. 3d, 4b). Collectively, the W327A, R328A, D329A, K352A,
205 N353A, and D354A mutations resulted in a marked reduction of both fluorescence intensity
206 and pseudovirus entry efficiency (Fig. 4b, c and Supplementary Fig. 11b). These residues are
207 located within the core of the receptor-binding motif, and the loss of function upon mutation
208 highlights their critical role in mediating the interaction between the HKU5 RBD and ACE2.
209 Sequence alignment of ACE2 orthologs from representative species revealed that, although
210 ACE2 is generally conserved among vertebrates, the key receptor-binding motifs (^{327}WRD^{329}
211 and ^{352}KND^{354}) are more conserved in avian species, exemplified by *Pitta sordida* (Hooded
212 Pitta) (Fig. 4d and Supplementary Fig. 10). The sequence identity of the PD of *Pitta sordida*
213 ACE2 (*Ps*PD) with *Pa*PD and *Hs*PD is 69% and 76%, respectively. Both pseudovirus infection
214 and cell–cell fusion assays demonstrated that Lenti-X 293T or Caco-2 cells stably expressing
215 *Pitta sordida* ACE2 (*Ps*ACE2) could robustly support HKU5 entry (Fig. 4e, f and
216 Supplementary Fig. 11). We measured the binding affinity of *Ps*PD for HKU5 RBD by BLI,

217 which yielded a dissociation constant (KD) of 122.9 ± 1.3 nM (Supplementary Fig. 12).

218 To analyze the impact of the receptor interface residue changes on HKU5 RBD recognition,
219 we solved the cryo-EM structure of the HKU5 RBD–*Ps*PD complex. Likely due to the reduced
220 affinity, a large fraction of the *Ps*PD molecules remained unbound in the 2D classification.
221 However, after collecting sufficient data, we solved the HKU5 RBD–*Ps*PD complex at a
222 resolution of 3.2 Å (Fig. 4g and Supplementary Fig. 13). *Ps*PD binds to the HKU5 RBD in a
223 manner similar to that of *Pa*PD (Supplementary Figs. 14, 15). The core interaction interface
224 between *Ps*PD and HKU5 RBD is maintained by the WRD and KND motifs in *Ps*PD, along
225 with other conserved residues (Fig. 4h-k). Some interface residues of *Ps*PD were mutated
226 relative to *Pa*PD, including Q25, D37, E325, G387, and P389, which correspond to R26, N38,
227 P324, N386, and S388 in *Pa*PD, respectively (Fig. 4d and Supplementary Fig. 15). The E325
228 in *Ps*PD (corresponding to P324 in *Pa*PD) disrupts its hydrophobic interaction with Y463 in
229 RBD but forms a hydrogen bond instead (Fig. 4k and Supplementary Fig. 15b). The E325 in
230 *Ps*PD forms a salt bridge with *Ps*PD R329 (corresponding to R328 in *Pa*PD), which causes a
231 conformational shift of *Ps*PD R329, disrupting the salt bridge between *Ps*PD R329 and D459
232 in RBD (Fig. 4k and Supplementary Fig. 15b). The R33 in *Ps*PD (corresponding to H34 in
233 *Pa*PD) forms new polar contacts with T514 and E551 of the HKU5 RBD (Fig. 4i and
234 Supplementary Fig. 15c). Additionally, *Ps*PD displays a glycosylation pattern distinct from
235 *Pa*PD. *Pa*PD carries multiple glycans (e.g., N53, N103, N215, N279, N386, N431, N545),
236 broadly distributed across its surface (Supplementary Fig. 14). In contrast, *Ps*PD has fewer
237 sites (N52, N78, N322, N546), which are more concentrated around the binding interface
238 (Supplementary Fig. 14). Notably, N322 in *Ps*PD is glycosylated and forms additional contacts

239 at the RBD–*Ps*PD interface (Fig. 4k and Supplementary Fig. 15d). These differences in
240 glycosylation distribution likely contribute to the distinct binding modes and affinities observed
241 for HKU5 RBD with *Pa*PD and *Ps*PD. Furthermore, compared to *Pa*PD, the overall structure
242 of *Ps*PD is positioned slightly farther from the RBD, disrupting certain polar interactions, such
243 as between *Pa*PD E37 and RBD K519 (Supplementary Fig. 15e).
244 To further investigate whether different HKU5 sub-clades affect RBD binding to *Ps*PD, we
245 measured the KD values of the RBD of BtPa-BetaCoV/GD2013, HKU5-3, and other HKU5-
246 related viruses for *Ps*PD, which were 137.8 ± 0.9 nM, 176.2 ± 1.4 nM, and 232.5 ± 2.0 nM,
247 respectively (Supplementary Fig. 12). These differences suggest that mutations in different
248 HKU5 strains may facilitate adaptation to ACE2 receptors from diverse species, potentially
249 enabling cross-species transmission.
250 We analyzed the conservation of the RBD binding interface on ACE2 between bat and human.
251 The results revealed substantial differences in the ^{327}WRD^{329} and ^{352}KND^{354} residues between
252 bat and human ACE2, which may limit the potential for HKU5 to bind to human ACE2 (Fig.
253 4d). Although the spillover risk of HKU5 to human is currently low, continuous monitoring is
254 warranted, especially in the context of viral evolution.
255 Together, these findings provide a comprehensive perspective on the structural, functional, and
256 evolutionary characteristics of HKU5, enhancing our understanding of its receptor-binding
257 specificity and potential for cross-species transmission.
258

259 **Discussion**

260 This study provides critical insights into the molecular mechanisms underlying HKU5 S

protein interaction with ACE2, shedding light on its structural adaptations, evolutionary dynamics, and the potential of cross-species transmission.

We identified two fatty acid molecules, oleic acid and palmitic acid, bound to the HKU5 S protein. These molecules stabilize the closed conformation of the S protein, likely modulating receptor accessibility. Similar to findings in other β-coronaviruses, including SARS-CoV-2[17] and HCoV-OC43[40], fatty acid binding occurs at conserved hydrophobic pockets within the RBD (Supplementary Table 1). Mutational analyses revealed that disruption of these interactions in HKU5 induces a structural shift toward a more relaxed conformation. This suggests that fatty acids play a crucial role in maintaining the closed state, potentially limiting premature receptor binding and aiding immune evasion. Notably, we identified a novel fatty acid binding pocket proximal to the RBM region in the HKU5 RBD. The cryo-EM map of the HKU5 RBD–*Pa*PD complex shows no density in this pocket, indicating that fatty acid binding may require the trimeric structure of the S protein. The regulatory mechanism aligns with prior studies proposing that fatty acid presence favors the "down" conformation of RBDs[41]. The widespread presence of fatty acids in coronaviral S proteins highlights their conserved role in regulating conformational dynamics. Efforts to design small-molecule inhibitors targeting these binding pockets have shown promise but require further structural optimization to enhance efficacy[42]. However, although cryo-EM and LC-MS identify oleic- and palmitic-acid binding at two sites on HKU5 S and pocket-disrupting mutations loosen the trimer, these substitutions did not cause a significant loss of pseudovirus entry. We infer that the fatty-acid pockets modulate the conformational equilibrium (stabilizing the closed state) without being obligatory for receptor engagement under our assay conditions.

283 Structural analysis revealed that the HKU5 RBD recognizes ACE2 through a unique
284 mechanism distinct from other ACE2-binding coronaviruses. Unlike the RBM regions of
285 SARS-CoV and SARS-CoV-2, which exhibit conserved ACE2-binding motifs[43], HKU5
286 demonstrates an entirely novel interaction interface. These findings illustrate the evolutionary
287 plasticity of coronaviruses and the convergent use of ACE2 by distinct lineages. Comparison
288 of the available S protein structures from HKU5, HKU5-2, HKU5-19s, and MRCoV
289 (Supplementary Fig. 16) shows a conserved closed conformation, while sequence
290 diversification is clustered at the ACE2-binding interface. In particular, HKU5-2 carries
291 substitutions within the RBM that may fine-tune receptor interactions, suggesting that
292 adaptation primarily targets the binding interface rather than the overall spike architecture.
293 The broad tissue expression and high conservation of ACE2 across mammalian species provide
294 a molecular basis for the cross-species transmission of coronaviruses[44,45]. Continuous
295 adaptation of viral S proteins enables optimization of ACE2 binding, as exemplified by the
296 progressive evolution of SARS-CoV-2 variants[46,47]. This interplay between receptor
297 conservation and viral adaptability emphasizes the critical role of ACE2 in shaping coronavirus
298 host range and transmission potential. Our analysis initially suggested that certain avian species,
299 such as *Pitta sordida*, harbor ACE2 variants capable of binding the HKU5 RBD, raising the
300 possibility of potential zoonotic reservoirs beyond mammals. In this study, we further
301 substantiated this prediction by performing pseudovirus entry and cell–cell fusion assays, both
302 of which demonstrated that cells stably expressing *Pitta sordida* ACE2 can indeed support
303 HKU5 entry. These findings provide functional evidence that avian ACE2 orthologs are not
304 only structurally compatible but also operationally competent to mediate HKU5 infection.

305 Traditionally, α- and β-coronaviruses are not thought to infect avian hosts, as birds are typically
306 reservoirs for γ- and δ-coronaviruses. Our data therefore represent an intriguing exception and
307 suggest that HKU5 has evolved a broader receptor usage than previously appreciated. This
308 observation challenges the conventional view of strict host–virus associations and raises the
309 possibility that certain avian species may, at least at the receptor level, serve as potential
310 conduits for cross-class transmission. Nevertheless, we emphasize that our results are based on
311 *in vitro* receptor reconstitution, and whether such interactions occur in natural settings will
312 require live virus studies and ecological surveillance to assess their biological relevance.

313 In summary, our findings advance the understanding of how coronaviruses adapt to diverse
314 hosts via ACE2 utilization, emphasizing the structural and functional diversity of this
315 interaction. By elucidating the roles of fatty acid-mediated conformational regulation and
316 ACE2 as a cross-species receptor, this study highlights the importance of monitoring HKU5
317 and related viruses for their zoonotic potential and public health implications.

318

319 **Methods**

320 **Protein preparation**

321 The extracellular domain (ECD) (1~1293 a.a.) of the S protein of BatCoV-HKU5 (UniProt ID:
322 A3EXD0) was cloned into the pCAG vector (Invitrogen) with a C-terminal T4 fibritin
323 trimerization motif followed by a Flag tag and a 10×His tag. A "GSAS" mutation at residues
324 742 to 745 was introduced into the S protein to prevent cleavage by host. Double mutants of
325 the S (S_{DM1}) protein were generated with a standard two-step PCR-based strategy. The RBD
326 domains of the S protein of different HKU5 sub-clades, including BatCoV-HKU5 (UniProt ID:

327 A3EXD0), BatCoV-HKU5-3 (GenBank accession: ABN10893.1), BtPa-BetaCoV/GD2013
328 (GenBank accession: AIA62343.1) and BatCoV-HKU5-Realted (GenBank accession:
329 QHA24687.1), were also cloned into the pCAG vector (Invitrogen) with an N-terminal signal
330 peptide for secretion and a C-terminal 10×His tag. The PD domains of ACE2 of different
331 species, including *Pipistrellus abramus* (UniProt ID: C7ECT9, *Pa*PD, 18~615 a.a.), *Pitta*
332 *sordida* (UniProt ID: A0A851FF99, *Ps*PD, 18~617 a.a.) and *Homo sapiens* (UniProt ID:
333 Q9BYF1, *Hs*PD, 25-622 a.a.), were also cloned into the pCAG vector (Invitrogen) with an N-
334 terminal signal peptide for secretion, followed by an N-terminal 2×StrepII tag and a C-terminal
335 10×His tag. All the plasmids used to transfect cells were prepared by GoldHi EndoFree Plasmid
336 Maxi Kit (CWBIO). The purification processes of these proteins were the same as those
337 described previously for the HKU1-B S protein[34]. Briefly, HEK293F mammalian cells
338 (Thermo Fisher Scientific, Cat# A14527) were cultured in SMM293-TII medium (Sino
339 Biological) at 37°C and 5% CO_2 in a Multitron-Pro shaker (Infors, 130 rpm). When the cell
340 density reached 2.0×10^6 cells/mL, the plasmid was transiently transfected into the cells. To
341 transfect one liter of cell culture, approximately 1.5 mg of plasmid was premixed with 3 mg of
342 polyethylenimine (PEI) (Yeasen Biotechnology) in 50 mL of fresh medium for 30 min before
343 being added to the cell culture. After 70 h of overexpression, cells were removed by
344 centrifugation at 4000×g for 15 min. The secreted proteins were purified by Ni-NTA Agarose
345 (GE Healthcare). After loading twice, the Ni-NTA Agarose was washed with the wash buffer
346 containing 25 mM Tris (pH 8.0), 150 mM NaCl, 50 mM imidazole. The protein was eluted
347 with the elute buffer containing 25 mM Tris (pH 8.0), 150 mM NaCl, 500 mM imidazole. The
348 eluate of RBDs or PDs was concentrated and subjected to size-exclusion chromatography (SEC,

349 Superdex 200 Increase 10/300 GL, GE Healthcare) in buffer containing 25 mM Tris (pH 8.0),
350 150 mM NaCl. The eluent of S or S_{DM1} protein was subjected to SEC (Superose 6 Increase
351 10/300 GL, GE Healthcare) in buffer containing 25 mM Tris (pH 8.0), 150 mM NaCl. The
352 HKU5 RBD was incubated with *Pa*PD or *Ps*PD at a molar ratio of about 5:1 for 1 h. Then the
353 mixtures were subjected to SEC (Superose 6 Increase 10/300 GL, GE Healthcare) in buffer
354 containing 25 mM Tris (pH 8.0), 150 mM NaCl. The peak fractions of SEC were collected and
355 concentrated for cryo-EM analysis.
356

357 **Cryo-EM sample preparation and data acquisition**

358 The protein samples were concentrated to ~2.5 mg/mL and applied to the grids. Aliquots (3.5
359 μL) of the protein were placed on glow-discharged holey carbon grids (Quantifoil Au R1.2/1.3).
360 The grids were blotted for 3.5 s and flash-frozen in liquid ethane cooled by liquid nitrogen
361 using the Vitrobot Mark IV (Thermo Fisher Scientific). The prepared grids were transferred to
362 a Krios (Thermo Fisher Scientific) operating at 300 kV equipped with a Gatan K3 detector and
363 GIF Quantum energy filter. Movie stacks were automatically collected using EPU software
364 (v3.11), with a slit width of 20 eV on the energy filter and a defocus range from -1.2 μm to -
365 2.2 μm in super-resolution mode at a nominal magnification of 81,000×. Each stack was
366 exposed for 2.56 s with an exposure time of 0.08 s per frame, resulting in a total of 32 frames
367 per stack. The total dose rate was ~50 $e^-/Å^2$ for each stack.
368

369 **Data processing**

370 The movie stacks were motion corrected with MotionCor2[48] and binned two fold, resulting in

371 a pixel size of 1.087 Å/pixel. Meanwhile, dose weighting was performed[49]. After patch CTF
372 estimation, particles were automatically picked according to the templates generated from an
373 initial 2D classification of manually picked particles by cryoSPARC (v4.6.2)[50]. After 2D
374 classification, the particles with clear features were selected and subjected to *ab-initio*
375 reconstruction to obtain the initial models, then multi-hetero refinements without symmetry
376 were performed to selected good particles using cryoSPARC (v4.6.2)[50]. The selected particles
377 were subjected to non-uniform refinement, local CTF refinement or global CTF refinement,
378 and local refinement, resulting in 3D reconstruction for the whole structure. The resolution was
379 estimated with the gold-standard Fourier shell correlation 0.143 criterion[51] with high-resolution
380 noise substitution[52]. Minor variations in processing were applied for different samples, as
381 detailed in Supplementary Figures 1, 4, 7, and 13. All of the map figures were generated in
382 ChimeraX (v1.3)[53] or Chimera (v1.16)[54].
383

384 **Model building and structure refinement**

385 The predicted atomic models generated by Alphafold 3[55] were used as templates and flexibly
386 fitted into the cryo-EM maps using molecular dynamics in VMD (v1.9.3)[56], followed by
387 manual adjustment with Coot (v0.8.9.2)[57] to obtain the atomic models. Each residue was
388 manually checked with the chemical properties taken into consideration during model building.
389 Several segments, whose corresponding densities were invisible, were not modeled.
390 Specifically, in both the HKU5 S protein and the S_{DM1} protein, the 739~750 a.a. at the S1/S2
391 cleavage site could not be modeled. In addition, 686~700 a.a. within SD2 of the HKU5 S
392 protein were not built. Structural refinement was performed in Phenix (v1.14)[58] with secondary

393 structure and geometry restraints to prevent overfitting (Supplementary Table 2).

394

395 **Generation of stable cell lines**

396 Full-length ACE2 from three species, *Pipistrellus abramus* (P.abr), *Pitta sordida* (P.sor), and
397 *Homo sapiens* (Human), were cloned into the lentiCRISPR v2 vector[59] with a spleen focus-
398 forming virus (SFFV) promoter, followed by a FLAG tag and linked via a P2A ribosome-
399 skipping site (ATNFSLLKQAGDVEENPGP) to an mCherry reporter at the C terminus.
400 Mutants of P.abr ACE2 were cloned using the same strategy. The lentiviral transfer plasmids
401 encoding full-length ACE2, together with the packaging vectors psPAX2 and pMD2.G, were
402 co-transfected into Lenti-X 293T cells (Takara Bio, Cat# 632180). Cells were maintained in
403 D10 medium (DMEM supplemented with 10% (v/v) FBS, 100 U/mL penicillin G, and 100
404 μg/mL streptomycin) at 37 °C in a water-saturated atmosphere containing 5% CO_2. Three days
405 after transfection, the supernatants were harvested, clarified by centrifugation at 1,000×g, and
406 filtered through 0.45 μm membranes (Beyotime). To concentrate lentivirus, protamine sulfate
407 (80 μg/mL, Macklin) and chondroitin sulfate C (80 μg/mL, Macklin) were added as described
408 previously[60]. Next, Lenti-X 293T or Caco-2 (ATCC, Cat# HTB-37) cells (1×10^6 per well in 1
409 mL D10) supplemented with 5 μg/mL polybrene (Beyotime) were transduced with 1 mL
410 concentrated lentivirus. Cells exhibiting comparable mCherry fluorescence intensity were
411 sorted on a MA900 Multi-Application Cell Sorter (Sony). Debris was excluded using FSC-A
412 versus SSC-A, singlets were selected using FSC-A versus FSC-H, and mCherry-positive cells
413 were gated in the 561-nm channel (610/20-nm filter). The sort gate was centered on the main
414 mCherry-positive population to ensure comparable expression across lines. Sorted cells were

415 used for subsequent experiments.

416

417 **Pseudovirus production and entry assays**

418 Full-length HKU5 (UniProt ID: A3EXD0) S proteins, with or without mutations, were cloned
419 into the pCAG vector (Invitrogen) with a C-terminal truncation (Δ13) followed by a 10×His
420 tag. Pseudoviruses (PSVs) were generated using the HIV-1 backbone plasmid pNL4-
421 3.Luc.$R^{-}E^{-}$[61], which encodes a luciferase reporter but lacks functional Env. Briefly, Lenti-X
422 293T cells were seeded into 10-cm dishes and co-transfected with pNL4-3.Luc.$R^{-}E^{-}$ (20 μg)
423 and HKU5 S plasmid (10 μg) using PEI (90 μg). Supernatants were harvested 48 h post-
424 transfection, clarified by centrifugation at 12,000×g for 10 min at 4 °C, aliquoted, and stored
425 at −80 °C.

426 For entry assays, Lenti-X 293T cells stably or transiently expressing indicated ACE2 orthologs
427 or mutants were seeded in 96-well plates (5×10^4 cells/well) and infected with PSVs in the
428 presence of polybrene (8 μg/mL, Beyotime) for 18 h. Before inoculation, PSVs produced in
429 Opti-MEM (Gibco) were treated with TPCK-trypsin (25 μg/mL, Sigma-Aldrich, T8802) at
430 room temperature for 10 min, and proteolytic activity was neutralized by FBS. Next, cells were
431 replenished with D10 medium, cultured for an additional 48 h, and then lysed with Cell Culture
432 Lysis 5× Reagent (Promega, diluted 1:5 in deionized water) at room temperature for 30 min.
433 Luciferase activity was then measured with the Luciferase Assay System (Promega, E1501)
434 using a Varioskan LUX multimode microplate reader (Thermo Fisher Scientific). All assays
435 were performed in triplicate, and data were analyzed and plotted using GraphPad Prism 10.1.2.

436

437 **Western blot**

438 Western blot was performed to examine the proteolytic processing and incorporation efficiency
439 of WT and mutant HKU5 S proteins. The PSV-containing supernatants were concentrated using
440 protamine sulfate (80 μg/mL, Macklin) and chondroitin sulfate C (80 μg/mL, Macklin). Viral
441 pellets were resuspended in Cell Culture Lysis 5× Reagent (Promega, diluted 1:5 in deionized
442 water) and incubated at room temperature for 10 min, followed by mixing with one-fifth of the
443 volume of 5×SDS loading buffer. Proteins were resolved by SDS–PAGE and probed using anti
444 His-Tag mouse monoclonal antibody (CWBIO, CW0286M; 1:2000) followed by goat anti-
445 mouse IgG secondary antibody (CWBIO, CW0102; 1:5000). Blots were washed three times
446 with TBST and visualized using the BeyoECL Plus (Beyotime, P0018S) with Amersham
447 Imager 680 (Cytiva).

448

449 **Bio-layer interferometry (BLI)**

450 BLI experiments were performed using the Octet system (ForteBio) to characterize the protein
451 interactions. StrepII-10×His-tagged *Pa*PD and *Ps*PD proteins, along with 10×His-RBD
452 proteins from four HKU5 strains, were purified separately. At room temperature, *Pa*PD
453 proteins were immobilized onto equilibrated streptavidin (SA) biosensors. Subsequently, the
454 biosensors were exposed to solutions containing various concentration of RBD proteins (0 nM,
455 12.5 nM, 25 nM, 50 nM, 100 nM, 200 nM, 400 nM, and 800 nM), with binding kinetics
456 monitored in real-time. Following the association phase, the biosensors were immersed in the
457 assay buffer to monitor dissociation kinetics in real-time. Sensorgrams were analyzed using
458 Octet Analysis Studio (v13.0) to determine the binding affinity constants between the PD and

459 RBD proteins. This process was repeated to evaluate the binding affinities between the two PD
460 proteins and the four RBD proteins. For the binding affinity measurements between *Ps*PD and
461 different RBDs, the RBD concentration gradient was set at 0 μM, 0.04 μM, 0.08 μM, 0.16 μM,
462 0.32 μM, 0.64 μM, 1.28 μM, and 2.56 μM.
463

464 **Tripartite split-fluorescence system**

465 We designed a tripartite split-fluorescence system containing plasmids A, B, and C. Plasmid A
466 encoded the first nine β-strands (1~196 a.a.) of sfGFP, followed by a stop codon and an internal
467 ribosome entry site 2 (iRES2) sequence to mediate the subsequent translation of iRFP702. For
468 plasmid B, the tenth β-strand of sfGFP (197~216 a.a.) was inserted at the N-terminus and fused
469 to the RBD via a linker (DVGGGGSEGGGSGGPGSGGEGSAGGGSAGGGS). An iRES2
470 sequence and mCherry sequence were then inserted downstream. For plasmid C, the PD was
471 inserted at the N-terminus and fused to the eleventh β-strand of sfGFP (217~238 a.a.) via a
472 linker (GSGAGGSPGGGSGGSGSSASGGSTSGGGSGGGS), followed by iRES2 and EBFP2
473 sequences. The designed sequences were synthesized by SynbioB and cloned into the
474 mammalian expression vector pCAG.
475

476 **Flow cytometry sorting and statistical analysis**

477 HEK293F cells were cultured in SMM293-TII medium (Sino Biological) at 37°C with 5% CO_2
478 under shaking conditions (120 rpm). Plasmid A, plasmid B expressing WT or mutant RBD,
479 and plasmid C expressing WT or mutant PD were mixed at a 1:1:1 ratio (5 μg each) and
480 transfected into cells (2×10^6 cells per 5 mL flask) using PEI at a 2:1 DNA-to-PEI mass ratio.

481 After 48 h, cells were harvested by centrifugation at 200×g for 2 min and washed twice with 2
482 mL PBS (Gibco) at room temperature. The final cell pellet was resuspended in 1ml PBS for
483 flow cytometry. Flow cytometry was performed on a BD FACSymphony™ A3 (BD
484 Biosciences). Single-cell populations were gated based on forward scatter area (FSC-A), side
485 scatter area (SSC-A), and forward scatter height (FSC-H) parameters. Cells co-expressing
486 plasmids A, B, and C, identified by simultaneous positivity in the BV421 (405 nm laser, 450/50
487 nm filter), BV711 (405 nm laser, 710/50 nm filter), and PE-CF594 (561 nm laser, 610/20 nm
488 filter) fluorescence channels, were analyzed for sfGFP fluorescence intensity in the FITC
489 channel (488 nm laser, 530/30 nm filter). The median fluorescence intensity of the gated
490 population was calculated using FlowJo (v10.6.2). All experiments were performed in triplicate.
491

492 **Immunofluorescence staining**

493 Immunofluorescence assays were performed to assess the expression of ACE2 orthologs and
494 mutants fused with FLAG tags. Transfected cells were fixed and permeabilized with 100%
495 methanol for 10 min at room temperature, incubated with mouse anti-DDDDK-tag mAb
496 (ABclonal, AE005; 1:200) diluted in PBS containing 1% BSA for 1 h at 37 °C, washed with
497 HBSS, and then incubated with ABflo® 647-conjugated goat anti-mouse IgG (ABclonal,
498 AS059; 1:150) for 1 h at 37 °C in the dark. Nuclei were stained with Hoechst 33342 (1:100
499 dilution in HBSS) for 30 min at 37 °C. Images were acquired using a CSU-W1 SoRa spinning
500 disk confocal system (Nikon) and processed with Fiji (ImageJ v1.54f).
501

502 **Cell–cell fusion assay**

503 Cell–cell fusion was performed in Caco-2 cells stably expressing ACE2 orthologs using a dual-
504 split protein (DSP) reporter system. To evaluate membrane fusion mediated by S glycoprotein-
505 ACE2, group A cells were transfected with HKU5 S and rLucN(1–155)-sfGFP1–7(1–157)
506 plasmids, while group B cells were transfected with HKU5 S and sfGFP8–11(158–231)-
507 rLuc(156–311). After 24 h, cells were trypsinized, mixed, and seeded into 96-well plates (8×10^4
508 cells/well). Following another 24 h of growth, cells were washed with DMEM and incubated
509 with or without TPCK-trypsin (Sigma-Aldrich, T8802) for 10 min at room temperature,
510 followed by immediate replenishment with D10 medium to neutralize trypsin. After 12 h,
511 nuclei were stained with Hoechst 33342 (1:100 dilution in HBSS) for 30 min at 37 °C, and
512 syncytia formation with green fluorescence was visualized using a CSU-W1 SoRa spinning
513 disk confocal system (Nikon) and processed with Fiji (ImageJ v1.54f).
514

515 **Data availability**

516 The atomic coordinates and cryo-EM maps generated in this study have been deposited in the
517 Protein Data Bank (http://www.rcsb.org) and the Electron Microscopy Data Bank
518 (https://www.ebi.ac.uk/pdbe/emdb/) under the following accession codes (PDB: 9KR8, 9KR9,
519 9KRA, 9KRB; EMDB: EMD-62522, EMD-62523, EMD-62524, EMD-62525, EMD-64945).
520 All other data supporting the findings of this study are available within the article and the
521 Supplementary Information. All materials used in this study are available from the
522 corresponding authors upon reasonable request. Source data are provided with this paper.
523

524 **References**

525 1 Fouchier, R. A. *et al.* Aetiology: Koch's postulates fulfilled for SARS virus. *Nature* **423**, 240,
526 doi:10.1038/423240a (2003).
527 2 Drosten, C. *et al.* Identification of a novel coronavirus in patients with severe acute respiratory syndrome.
528 *N Engl J Med* **348**, 1967-1976, doi:10.1056/NEJMoa030747 (2003).
529 3 Wu, F. *et al.* A new coronavirus associated with human respiratory disease in China. *Nature* **579**, 265-
530 269, doi:10.1038/s41586-020-2008-3 (2020).
531 4 Zhou, P. *et al.* A pneumonia outbreak associated with a new coronavirus of probable bat origin. *Nature*
532 **579**, 270-273, doi:10.1038/s41586-020-2012-7 (2020).
533 5 Ruiz-Aravena, M. *et al.* Ecology, evolution and spillover of coronaviruses from bats. *Nature Reviews*
534 *Microbiology* **20**, 299-314, doi:10.1038/s41579-021-00652-2 (2022).
535 6 Mackenzie, J. S., Childs, J. E., Field, H. E., Wang, L. F. & Breed, A. C. *The Role of Bats as Reservoir Hosts*
536 *of Emerging Neuroviruses*. (Neurotropic Viral Infections. 2016 Apr 8:403-54. doi: 10.1007/978-3-319-
537 33189-8_12.).
538 7 Letko, M., Seifert, S. N., Olival, K. J., Plowright, R. K. & Munster, V. J. Bat-borne virus diversity, spillover
539 and emergence. *Nature Reviews Microbiology* **18**, 461-471, doi:10.1038/s41579-020-0394-z (2020).
540 8 Jackson, C. B., Farzan, M., Chen, B. & Choe, H. Mechanisms of SARS-CoV-2 entry into cells. *Nat Rev Mol*
541 *Cell Biol* **23**, 3-20, doi:10.1038/s41580-021-00418-x (2022).
542 9 Benton, D. J. *et al.* Receptor binding and priming of the spike protein of SARS-CoV-2 for membrane fusion.
543 *Nature* **588**, 327-330, doi:10.1038/s41586-020-2772-0 (2020).
544 10 Gui, M. *et al.* Cryo-electron microscopy structures of the SARS-CoV spike glycoprotein reveal a
545 prerequisite conformational state for receptor binding. *Cell Res* **27**, 119-129, doi:10.1038/cr.2016.152
546 (2017).
547 11 Wrapp, D. *et al.* Cryo-EM structure of the 2019-nCoV spike in the prefusion conformation. *Science* **367**,
548 1260-1263, doi:10.1126/science.abb2507 (2020).
549 12 Ke, Z. *et al.* Structures and distributions of SARS-CoV-2 spike proteins on intact virions. *Nature* **588**, 498-
550 502, doi:10.1038/s41586-020-2665-2 (2020).
551 13 Nguyen, L. *et al.* Sialic acid-containing glycolipids mediate binding and viral entry of SARS-CoV-2. *Nature*
552 *Chemical Biology* **18**, 81-90, doi:10.1038/s41589-021-00924-1 (2022).
553 14 Pronker, M. F. *et al.* Sialoglycan binding triggers spike opening in a human coronavirus. *Nature* **624**, 201-
554 206, doi:10.1038/s41586-023-06599-z (2023).
555 15 Hulswit, R. J. G. *et al.* Human coronaviruses OC43 and HKU1 bind to 9-O-acetylated sialic acids via a
556 conserved receptor-binding site in spike protein domain A. *Proc Natl Acad Sci U S A* **116**, 2681-2690,
557 doi:10.1073/pnas.1809667116 (2019).
558 16 Qing, E., Hantak, M., Perlman, S. & Gallagher, T. Distinct Roles for Sialoside and Protein Receptors in
559 Coronavirus Infection. *mBio* **11**, doi:10.1128/mBio.02764-19 (2020).
560 17 Toelzer, C. *et al.* Free fatty acid binding pocket in the locked structure of SARS-CoV-2 spike protein.
561 *Science* **370**, 725-730, doi:10.1126/science.abd3255 (2020).
562 18 de Groot, R. J. *et al.* Middle East respiratory syndrome coronavirus (MERS-CoV): announcement of the
563 Coronavirus Study Group. *J Virol* **87**, 7790-7792, doi:10.1128/jvi.01244-13 (2013).
564 19 Lau, S. K. *et al.* Genetic characterization of Betacoronavirus lineage C viruses in bats reveals marked
565 sequence divergence in the spike protein of pipistrellus bat coronavirus HKU5 in Japanese pipistrelle:
566 implications for the origin of the novel Middle East respiratory syndrome coronavirus. *J Virol* **87**, 8638-

8650, doi:10.1128/jvi.01055-13 (2013).

20 Woo, P. C., Lau, S. K., Li, K. S., Tsang, A. K. & Yuen, K. Y. Genetic relatedness of the novel human group C betacoronavirus to Tylonycteris bat coronavirus HKU4 and Pipistrellus bat coronavirus HKU5. *Emerg Microbes Infect* **1**, e35, doi:10.1038/emi.2012.45 (2012).

21 Woo, P. C. Y. *et al.* Molecular diversity of coronaviruses in bats. *Virology* **351**, 180-187, doi:https://doi.org/10.1016/j.virol.2006.02.041 (2006).

22 Chen, J. *et al.* Bat-infecting merbecovirus HKU5-CoV lineage 2 can use human ACE2 as a cell entry receptor. *Cell* **188**, 1729-1742.e1716, doi:10.1016/j.cell.2025.01.042 (2025).

23 Zhao, J. *et al.* Farmed fur animals harbour viruses with zoonotic spillover potential. *Nature* **634**, 228-233, doi:10.1038/s41586-024-07901-3 (2024).

24 Park, Y. J. *et al.* Molecular basis of convergent evolution of ACE2 receptor utilization among HKU5 coronaviruses. *Cell* **188**, 1711-1728.e1721, doi:10.1016/j.cell.2024.12.032 (2025).

25 Catanzaro, N. J. *et al.* ACE2 from Pipistrellus abramus bats is a receptor for HKU5 coronaviruses. *Nat Commun* **16**, 4932, doi:10.1038/s41467-025-60286-3 (2025).

26 Li, W. *et al.* Angiotensin-converting enzyme 2 is a functional receptor for the SARS coronavirus. *Nature* **426**, 450-454, doi:10.1038/nature02145 (2003).

27 Hoffmann, M. *et al.* SARS-CoV-2 Cell Entry Depends on ACE2 and TMPRSS2 and Is Blocked by a Clinically Proven Protease Inhibitor. *Cell* **181**, 271-280.e278, doi:10.1016/j.cell.2020.02.052 (2020).

28 Hofmann, H. *et al.* Human coronavirus NL63 employs the severe acute respiratory syndrome coronavirus receptor for cellular entry. *Proc Natl Acad Sci U S A* **102**, 7988-7993, doi:10.1073/pnas.0409465102 (2005).

29 Ma, C. B. *et al.* Multiple independent acquisitions of ACE2 usage in MERS-related coronaviruses. *Cell* **188**, 1693-1710.e1618, doi:10.1016/j.cell.2024.12.031 (2025).

30 Ma, C. *et al.* Identification of ACE2 as the Entry Receptor for Two Novel European Bat Merbecoviruses. *bioRxiv*, 2023.2010.2002.560486, doi:10.1101/2023.10.02.560486 (2023).

31 Liu, C. *et al.* ACE2 utilization of HKU25 clade MERS-related coronaviruses with broad geographic distribution. *bioRxiv*, doi:10.1101/2025.02.19.639017 (2025).

32 Medina-Enríquez, M. M. *et al.* ACE2: the molecular doorway to SARS-CoV-2. *Cell Biosci* **10**, 148, doi:10.1186/s13578-020-00519-8 (2020).

33 Yuan, Y. *et al.* Cryo-EM structures of MERS-CoV and SARS-CoV spike glycoproteins reveal the dynamic receptor binding domains. *Nat Commun* **8**, 15092, doi:10.1038/ncomms15092 (2017).

34 Xia, L., Zhang, Y. & Zhou, Q. Structural basis for the recognition of HCoV-HKU1 by human TMPRSS2. *Cell Res* **34**, 526-529, doi:10.1038/s41422-024-00958-9 (2024).

35 Staufer, O. *et al.* Synthetic virions reveal fatty acid-coupled adaptive immunogenicity of SARS-CoV-2 spike glycoprotein. *Nature Communications* **13**, 868, doi:10.1038/s41467-022-28446-x (2022).

36 Yan, R. *et al.* Structural basis for the different states of the spike protein of SARS-CoV-2 in complex with ACE2. *Cell Res* **31**, 717-719, doi:10.1038/s41422-021-00490-0 (2021).

37 Xiong, Q. *et al.* Close relatives of MERS-CoV in bats use ACE2 as their functional receptors. *Nature* **612**, 748-757, doi:10.1038/s41586-022-05513-3 (2022).

38 Starr, T. N. *et al.* ACE2 binding is an ancestral and evolvable trait of sarbecoviruses. *Nature* **603**, 913-918, doi:10.1038/s41586-022-04464-z (2022).

39 Chakrabarti, S. *et al.* Touch sensation requires the mechanically gated ion channel ELKIN1. *Science* **383**, 992-998, doi:10.1126/science.adl0495 (2024).

40 Bangaru, S. *et al.* Structural mapping of antibody landscapes to human betacoronavirus spike proteins.

611 *Sci Adv* **8**, eabn2911, doi:10.1126/sciadv.abn2911 (2022).
612 41 Hills, F. R. *et al.* Variation in structural motifs within SARS-related coronavirus spike proteins. *PLoS*
613 *Pathog* **20**, e1012158, doi:10.1371/journal.ppat.1012158 (2024).
614 42 Wang, Q. *et al.* In Silico Discovery of Small Molecule Modulators Targeting the Achilles' Heel of SARS-
615 CoV-2 Spike Protein. *ACS Cent Sci* **9**, 252-265, doi:10.1021/acscentsci.2c01190 (2023).
616 43 Yan, R. *et al.* Structural basis for the recognition of SARS-CoV-2 by full-length human ACE2. *Science* **367**,
617 1444-1448, doi:10.1126/science.abb2762 (2020).
618 44 Damas, J. *et al.* Broad Host Range of SARS-CoV-2 Predicted by Comparative and Structural Analysis of
619 ACE2 in Vertebrates. *bioRxiv*, doi:10.1101/2020.04.16.045302 (2020).
620 45 Ma, C.-B. *et al.* Multiple independent acquisitions of ACE2 usage in MERS-related coronaviruses. *bioRxiv*,
621 2023.2010.2002.560486, doi:10.1101/2023.10.02.560486 (2024).
622 46 Li, L. *et al.* Structural basis of human ACE2 higher binding affinity to currently circulating Omicron SARS-
623 CoV-2 sub-variants BA.2 and BA.1.1. *Cell* **185**, 2952-2960.e2910, doi:10.1016/j.cell.2022.06.023 (2022).
624 47 Feng, L. *et al.* Structural and molecular basis of the epistasis effect in enhanced affinity between SARS-
625 CoV-2 KP.3 and ACE2. *bioRxiv*, 2024.2009.2003.610799, doi:10.1101/2024.09.03.610799 (2024).
626 48 Zheng, S. Q. *et al.* MotionCor2: anisotropic correction of beam-induced motion for improved cryo-
627 electron microscopy. *Nat Methods* **14**, 331-332, doi:10.1038/nmeth.4193 (2017).
628 49 Grant, T. & Grigorieff, N. Measuring the optimal exposure for single particle cryo-EM using a 2.6 Å
629 reconstruction of rotavirus VP6. *Elife* **4**, e06980, doi:10.7554/eLife.06980 (2015).
630 50 Punjani, A., Rubinstein, J. L., Fleet, D. J. & Brubaker, M. A. cryoSPARC: algorithms for rapid unsupervised
631 cryo-EM structure determination. *Nat Methods* **14**, 290-296, doi:10.1038/nmeth.4169 (2017).
632 51 Rosenthal, P. B. & Henderson, R. Optimal determination of particle orientation, absolute hand, and
633 contrast loss in single-particle electron cryomicroscopy. *J Mol Biol* **333**, 721-745,
634 doi:10.1016/j.jmb.2003.07.013 (2003).
635 52 Chen, S. *et al.* High-resolution noise substitution to measure overfitting and validate resolution in 3D
636 structure determination by single particle electron cryomicroscopy. *Ultramicroscopy* **135**, 24-35,
637 doi:10.1016/j.ultramic.2013.06.004 (2013).
638 53 Pettersen, E. F. *et al.* UCSF ChimeraX: Structure visualization for researchers, educators, and developers.
639 *Protein Sci* **30**, 70-82, doi:10.1002/pro.3943 (2021).
640 54 Pettersen, E. F. *et al.* UCSF Chimera--a visualization system for exploratory research and analysis. *J*
641 *Comput Chem* **25**, 1605-1612, doi:10.1002/jcc.20084 (2004).
642 55 Abramson, J. *et al.* Accurate structure prediction of biomolecular interactions with AlphaFold 3. *Nature*
643 **630**, 493-500, doi:10.1038/s41586-024-07487-w (2024).
644 56 Trabuco, L. G., Villa, E., Mitra, K., Frank, J. & Schulten, K. Flexible fitting of atomic structures into electron
645 microscopy maps using molecular dynamics. *Structure* **16**, 673-683, doi:10.1016/j.str.2008.03.005
646 (2008).
647 57 Emsley, P., Lohkamp, B., Scott, W. G. & Cowtan, K. Features and development of Coot. *Acta Crystallogr*
648 *D Biol Crystallogr* **66**, 486-501, doi:10.1107/s0907444910007493 (2010).
649 58 Adams, P. D. *et al.* PHENIX: a comprehensive Python-based system for macromolecular structure
650 solution. *Acta Crystallogr D Biol Crystallogr* **66**, 213-221, doi:10.1107/s0907444909052925 (2010).
651 59 Sanjana, N. E., Shalem, O. & Zhang, F. Improved vectors and genome-wide libraries for CRISPR screening.
652 *Nat Methods* **11**, 783-784, doi:10.1038/nmeth.3047 (2014).
653 60 Lee, J. Y. & Lee, H. H. A new chemical complex can rapidly concentrate lentivirus and significantly
654 enhance gene transduction. *Cytotechnology* **70**, 193-201, doi:10.1007/s10616-017-0133-0 (2018).

655 61 Connor, R. I., Chen, B. K., Choe, S. & Landau, N. R. Vpr is required for efficient replication of human
656 immunodeficiency virus type-1 in mononuclear phagocytes. *Virology* **206**, 935-944,
657 doi:10.1006/viro.1995.1016 (1995).

658

659 **Acknowledgements**

660 This work is supported by National Natural Science Foundation of China (82241081), the Key
661 Regional Research and Development Program (2023CSJZN0600) from Ministry of Science
662 and Technology of China, and State Key Laboratory of Gene Expression. We thank the staff of
663 the cryo-EM facility, the high-performance computing center, the mass spectrometry and
664 metabolomics core facility, the flow cytometry core facility, the protein characterization and
665 crystallography facility, and the microscopy imaging platform of Westlake University for
666 technical assistance, advice, and support. We also thank Dr. Xu Li and Dr. Peihan Wu for
667 providing materials and technical assistance for pseudovirus preparation.

668 **Author contributions**

669 Q.Z. and L.X. conceived the project. Y.Z., L.X., Y.L., W.G., and D.L. performed the
670 experiments. Y.Z. and L.X. analyzed the PDB structures and performed data visualization. All
671 authors contributed to data analysis. Q.Z., L.X., and Y.Z. wrote the manuscript. Q.Z. supervised
672 the project.

673 **Competing interests**

674 The authors declare no competing interests.

675

676 **Fig. 1. Cryo-EM structure of the HKU5 S protein.**

677 **a,** Cryo-EM map shown in side view (Left) at a contour level of 4 σ and the atomic model
678 shown in top view (Middle) of the HKU5 S protein, with protomers displayed in marine blue,
679 purple, and forest green, respectively. Enlarged views of the boxed regions in the middle panel,
680 showing the bound fatty acids (Right), with cryo-EM map shown at a contour level of 3 σ for
681 palmitic acid (orange) and 4 σ for oleic acid (yellow), respectively. **b-c,** Liquid
682 chromatography-mass spectrometry (LC-MS) analysis of purified HKU5 S protein. Top:
683 Chromatograms of C18 and C16 fatty acids. Bottom: Corresponding electrospray ionization
684 time-of-flight (ESI-TOF) mass spectra, with molecular weights of C18H32O2 and C16H34O2
685 labeled. Intens., intensity; m/z, mass/charge ratio. **d-e,** Binding pockets of oleic acid (**d**) and
686 palmitic acid (**e**) within the HKU5 S protein, highlighting key residues involved in polar
687 interactions, with hydrophobic residues in pocket 1 (F393, L419, L422, L423, F426, V428,
688 F431, P438, L441, L449, V451, V488, A490, F569, V571) and pocket 2 (P402, P403, I404,
689 A455, P502). All residues are shown as sticks.

690 **Fig. 2. Interactions between HKU5 RBD and bat ACE2.**

691 **a,** Cryo-EM map (Left) at a contour level of 4 σ and atomic model shown in cartoon (Right) of
692 HKU5 RBD (marine blue) in complex with *Pa*PD (orange). **b,** Enlarged view of the interaction
693 interface, showing *Pa*PD α1, α2, α3 helices, β-hairpin, and L_A loop interacting with β-strands
694 5~8 and the α4 of HKU5 RBD. **c-e,** Detailed analysis of the binding interface between HKU5
695 RBD and *Pa*PD, with polar interactions indicated by dashed black lines. **f,** ACE2 binding
696 modes for SARS-CoV-2, HCoV-NL63, PDF-2180, MOW15-22 and HKU5. *Hs*PD, *Pp*PD,
697 *Pd*PD and *Pa*PD are the peptidase domains of *Homo sapiens*, *Pipistrellus pipistrellus*,
698 *Pteronotus davyi* and *Pipistrellus abramus*, respectively. **g,** Superimposed ACE2 binding sites
699 of SARS-CoV-2, HCoV-NL63, PDF-2180, MOW15-22 and HKU5 on *Pa*PD. For clarity, other
700 PDs are not shown. Binding footprints are shown in cyan (MOW15-22), green (SARS-CoV-
701 2), violet (HCoV-NL63), red (PDF-2180) and marine blue (HKU5), respectively.

702

703 **Fig. 3. Interaction and functional analysis of HKU5 sub-clades RBDs with *Pa*PD.**

704 **a,** Binding and dissociation kinetics of RBDs of four HKU5 sub-clades (BatCoV-HKU5
705 (UniProt ID: A3EXD0), BatCoV-HKU5-3 (GenBank accession: ABN10893.1), BtPa-
706 BetaCoV/GD2013 (GenBank accession: AIA62343.1), and BatCoV-HKU5-Related (GenBank
707 accession: QHA24687.1)) with *Pa*PD measured by biolayer interferometry (BLI). R^2 values
708 are 0.9776, 0.9830, 0.9867, and 0.9861, respectively. **b,** Experimental schematic of tripartite
709 split-fluorescence system to evaluate HKU5 RBD-*Pa*PD interactions. **c,** Flow cytometry-based
710 sorting strategy for single-cell populations co-expressing HKU5 RBD and *Pa*PD. The first gate
711 (P1) was applied to exclude cell debris, followed by the second gate (P2) to remove doublets
712 or adhered cells. Populations P3 and P4 were subsequently defined based on fluorescence
713 intensity, and cells in P3 and P4 were isolated. sfGFP fluorescence intensity was quantified in
714 the P4 population. **d,** Relative sfGFP fluorescence intensity for WT or mutant HKU5 RBDs
715 binding *Pa*PD, normalized to the WT signal. Data represent mean ± standard deviation (SD)
716 from three independent experiments (n = 3). Source data are provided as a Source Data file.
717

718 **Fig. 4. Mutational analysis of ACE2 interface residues and cross-species RBD interactions.**
719 **a,** Critical interface residues of *Pa*PD involved in HKU5 RBD binding. **b,** Effects of *Pa*PD,
720 *Ps*PD, *Hs*PD and *Pa*PD mutants on HKU5 RBD binding, evaluated by flow cytometry and
721 tripartite split-fluorescence-based assays. The sfGFP fluorescence intensity was normalized to
722 WT *Pa*PD. Data represent mean ± SD from three independent experiments (n = 3). **c,** HKU5 S
723 pseudovirus (PSV) entry into Lenti-X 293T cells transiently expressing the indicated
724 *Pipistrellus abramus* ACE2 (*Pa*ACE2) mutants. Data represent mean ± SD of four technical
725 replicates from one representative experiment (three independent experiments performed in
726 total). **d,** Conservation analysis of *Pipistrellus abramus* (*Pa*PD) interface residues in *Homo*
727 *sapiens* (*Hs*PD) and *Pitta sordida* (*Ps*PD), highlighting conserved residues essential for cross-
728 species interactions. **e,** Entry of HKU5 S pseudovirus (PSV) into Lenti-X 293T cells stably
729 transfected with three ACE2 orthologs, *Pipistrellus abramus* (P.abr), *Pitta sordida* (P.sor) and
730 *Homo sapiens* (Human). Data represent mean ± SD of four technical replicates from one
731 representative experiment (three independent experiments performed in total). **f,** HKU5 S-
732 mediated cell–cell fusion using Caco-2 cells stably expressing the indicated ACE2 orthologs,
733 *Homo sapiens* (*Hs*ACE2), *Pipistrellus abramus* (*Pa*ACE2) and *Pitta sordida* (*Ps*ACE2), with
734 or without the addition of 10 μg/mL TPCK-treated trypsin. Untransfected Caco-2 cells under
735 the same conditions served as the blank control. Representative images from three independent
736 experiments showing similar results. **g,** Cryo-EM map (Left) at a contour level of 4 σ and
737 atomic model shown in cartoon (Right) of HKU5 RBD (marine blue) in complex with *Ps*PD
738 (purple). **h,** Enlarged view of the interaction interface between HKU5 RBD and *Ps*PD. **i-k,**
739 Detailed analysis of interface interactions between *Ps*PD and HKU5 RBD, with polar

interactions indicated by dashed black lines. Statistical significance was determined using two-sided unpaired Student's *t*-tests. ns, not significant ($P \geq 0.05$); * $P < 0.05$; ** $P < 0.01$; *** $P < 0.001$; **** $P < 0.0001$. Source data are provided as a Source Data file.

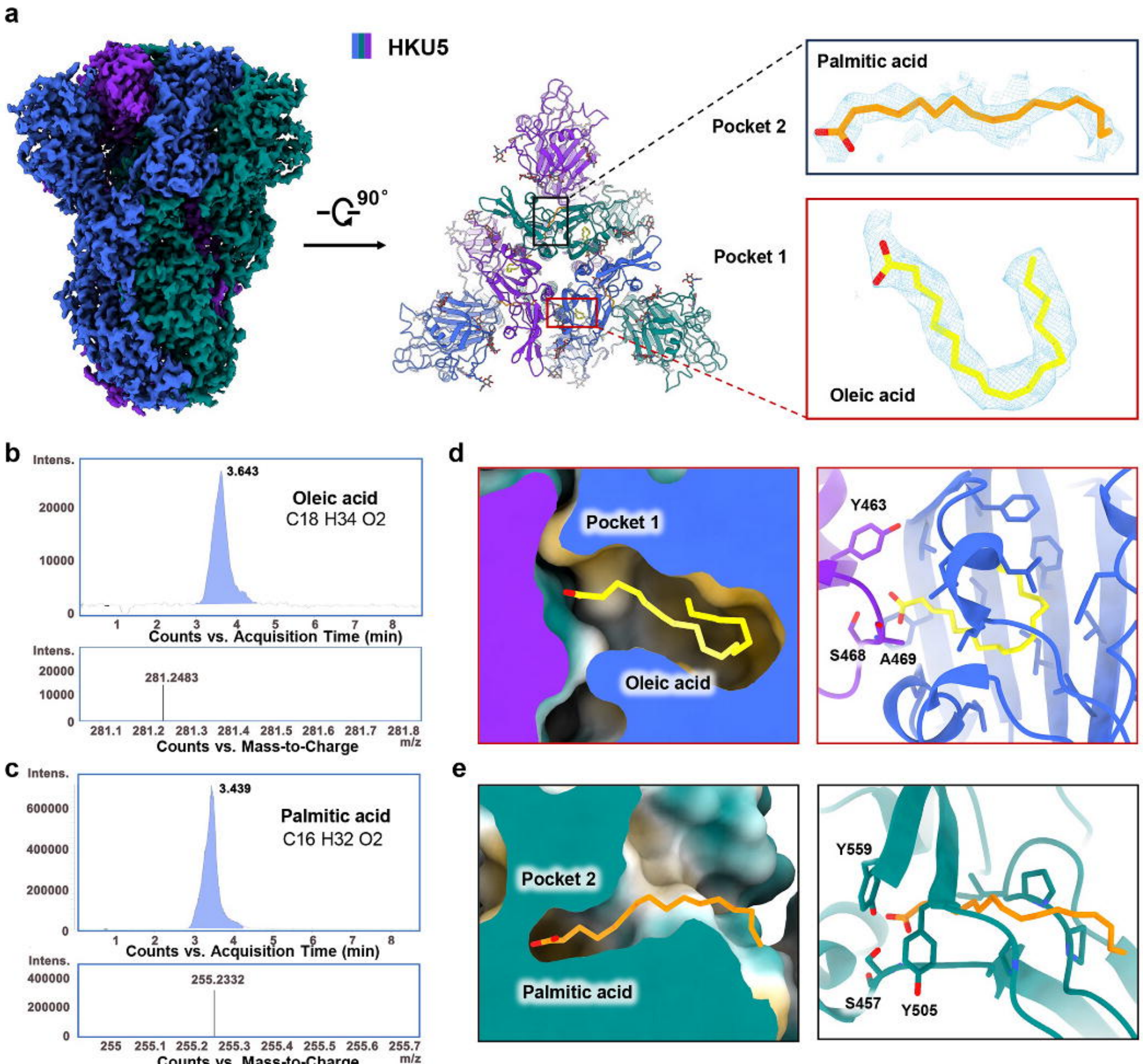
a
HKU5
90°
Pocket 2
Palmitic acid
Pocket 1
Oleic acid
b
Intens.
3.643
Oleic acid
C18 H34 O2
Counts vs. Acquisition Time (min)
281.2483
Counts vs. Mass-to-Charge
m/z
c
3.439
Palmitic acid
C16 H32 O2
Counts vs. Acquisition Time (min)
255.2332
Counts vs. Mass-to-Charge
d
Pocket 1
Oleic acid
Y463
S468
A469
e
Pocket 2
Palmitic acid
Y559
S457
Y505

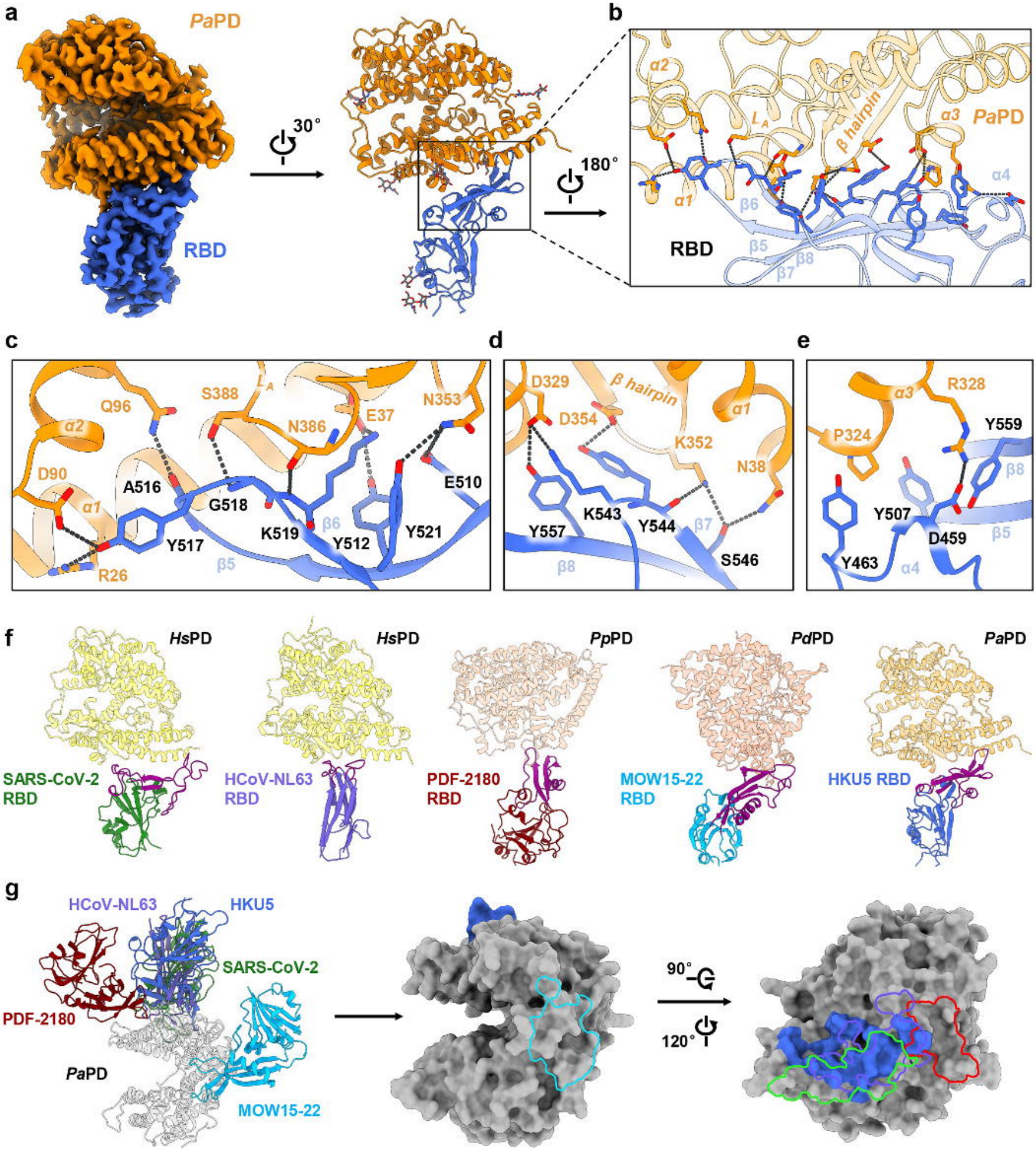
a
PaPD
RBD
30°
b
180°
α2
L_A
β hairpin
α3
PaPD
α4
α1
β6
RBD
β5
β8
β7
c
Q96
S388
L_A
N353
α2
N386
E37
D90
A516
E510
α1
G518
K519
β6
Y521
Y517
Y512
β5
R26
d
D329
β hairpin
D354
α1
K352
N38
K543
Y544
β7
Y557
S546
β8
e
α3
R328
Y559
P324
β8
Y507
D459
β5
Y463
α4
f
HsPD
HsPD
PpPD
PdPD
PaPD
SARS-CoV-2 RBD
HCoV-NL63 RBD
PDF-2180 RBD
MOW15-22 RBD
HKU5 RBD
g
HCoV-NL63
HKU5
SARS-CoV-2
PDF-2180
PaPD
MOW15-22
90°
120°

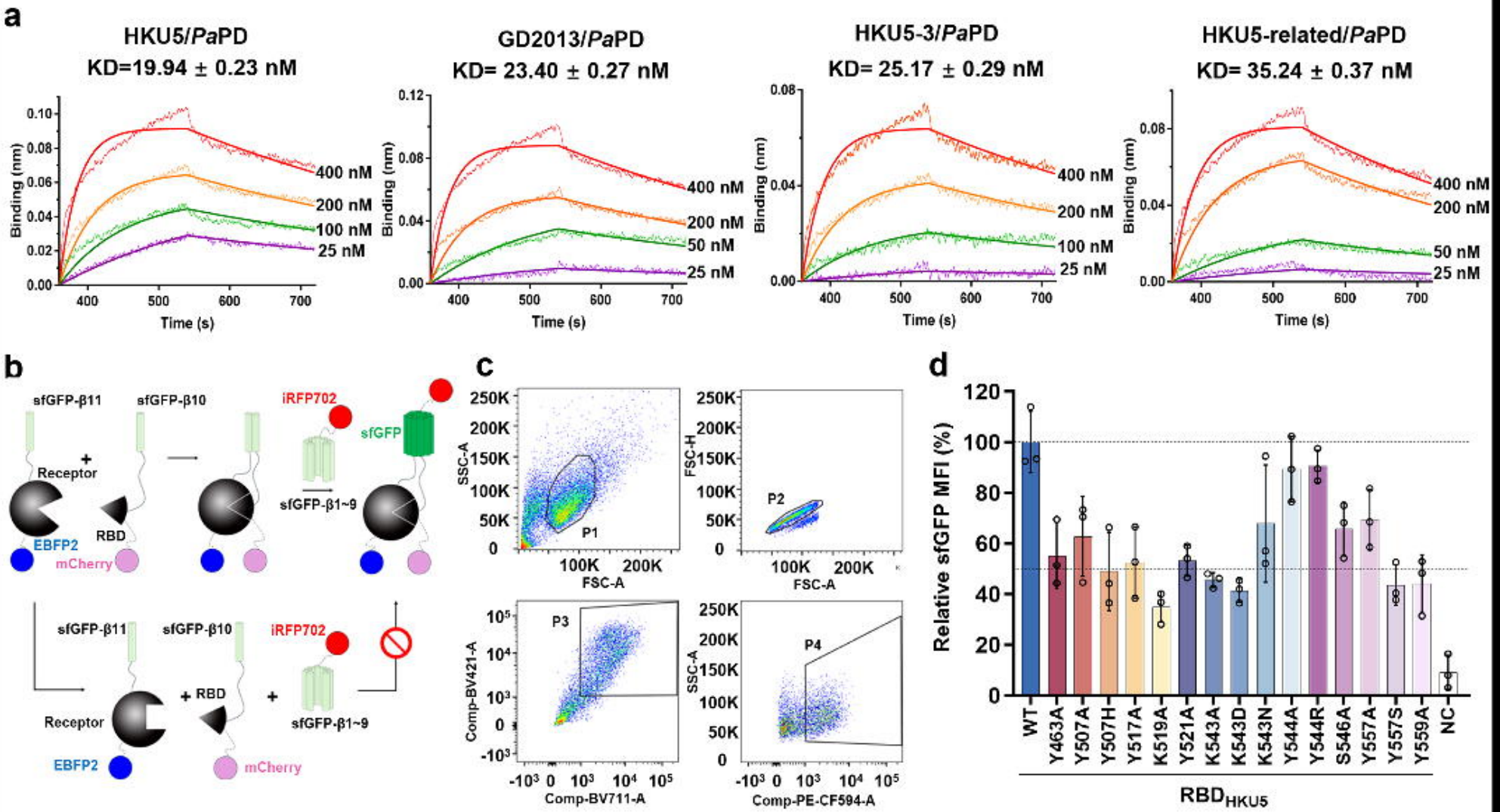
a
HKU5/PaPD
KD=19.94 ± 0.23 nM
GD2013/PaPD
KD= 23.40 ± 0.27 nM
HKU5-3/PaPD
KD= 25.17 ± 0.29 nM
HKU5-related/PaPD
KD= 35.24 ± 0.37 nM
Binding (nm)
Time (s)
400 nM
200 nM
100 nM
50 nM
25 nM
b
sfGFP-β11
sfGFP-β10
iRFP702
sfGFP
Receptor
RBD
EBFP2
mCherry
sfGFP-β1~9
c
SSC-A
FSC-A
FSC-H
P1
P2
P3
P4
Comp-BV421-A
Comp-BV711-A
Comp-PE-CF594-A
d
Relative sfGFP MFI (%)
WT
Y463A
Y507A
Y507H
Y517A
K519A
Y521A
K543A
K543D
K543N
Y544A
Y544R
S546A
Y557A
Y557S
Y559A
NC
RBD HKU5

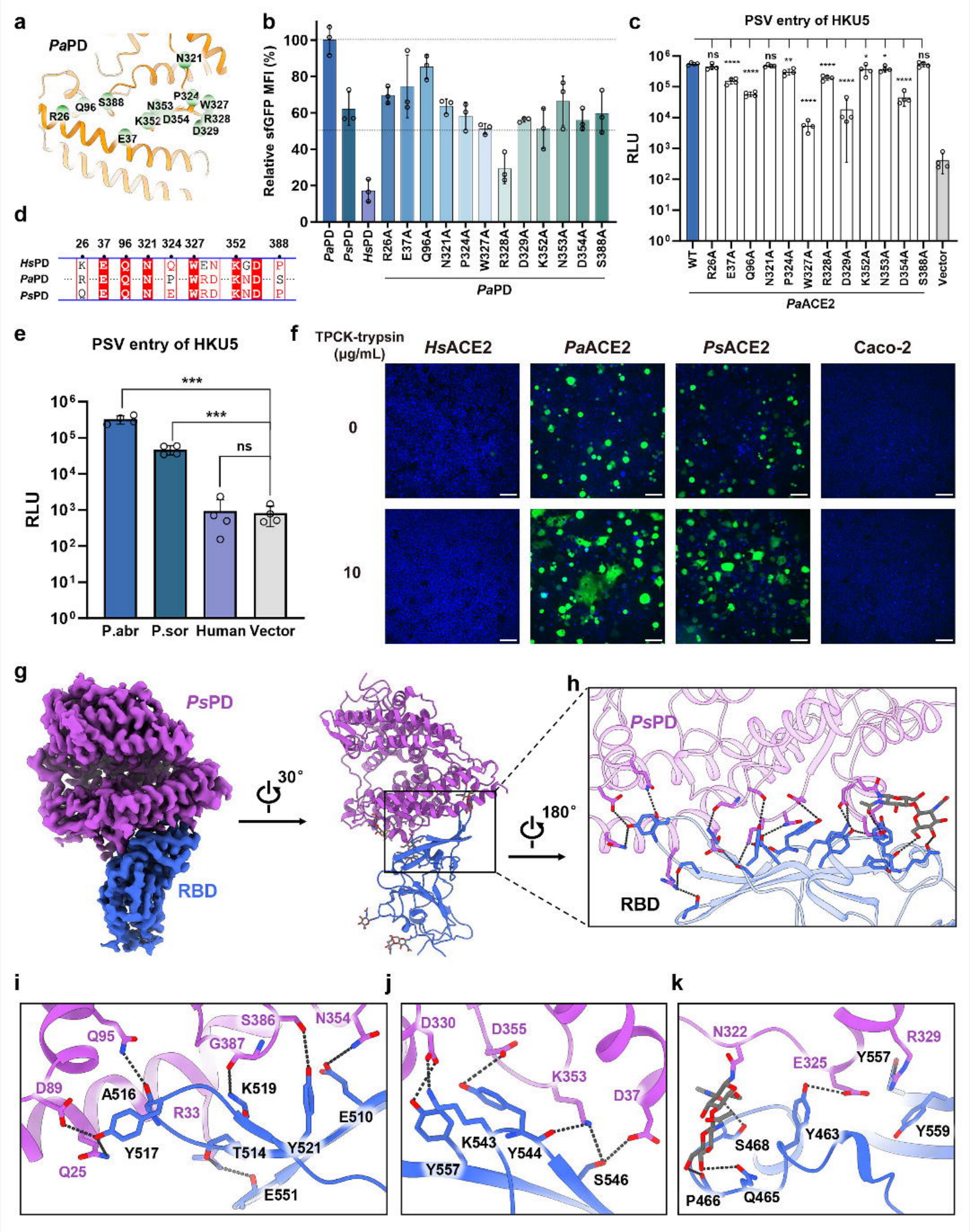
a
PaPD
N321
P324
S388
Q96
N353
W327
R26
K352
D354
R328
D329
E37
b
Relative sfGFP MFI (%)
PaPD
PsPD
HsPD
R26A
E37A
Q96A
N321A
P324A
W327A
R328A
D329A
K352A
N353A
D354A
S388A
PaPD
c
PSV entry of HKU5
RLU
WT
R26A
E37A
Q96A
N321A
P324A
W327A
R328A
D329A
K352A
N353A
D354A
S388A
Vector
PaACE2
d
26 37 96 321 324 327 352 388
HsPD
PaPD
PsPD
e
PSV entry of HKU5
RLU
P.abr
P.sor
Human
Vector
f
TPCK-trypsin (μg/mL)
HsACE2
PaACE2
PsACE2
Caco-2
0
10
g
PsPD
RBD
30°
h
PsPD
RBD
180°
i
Q95
S386
N354
G387
D89
A516
K519
R33
E510
Y517
T514
Y521
Q25
E551
j
D330
D355
K353
D37
K543
Y544
Y557
S546
k
N322
R329
E325
Y557
Y463
Y559
S468
P466
Q465